

Published in final edited form as:

Nat Chem. 2021 July 01; 13(7): 643–650. doi:10.1038/s41557-021-00688-0.

## Constructing ion-channels from water-soluble $\alpha$ -helical barrels

Alistair J. Scott<sup>#1</sup>, Ai Niitsu<sup>#1,2</sup>, Huong T. Kratochvil<sup>3</sup>, Eric J. M. Lang<sup>1</sup>, Jason T. Sengel<sup>4</sup>, William M. Dawson<sup>1</sup>, Kozhinjampara R. Mahendran<sup>5,6</sup>, Marco Mravic<sup>3</sup>, Andrew R. Thomson<sup>1,7</sup>, R. Leo Brady<sup>8,9</sup>, Lijun Liu<sup>10,11</sup>, Adrian J. Mulholland<sup>1,9</sup>, Hagan Bayley<sup>5</sup>, William F. DeGrado<sup>3</sup>, Mark I. Wallace<sup>4</sup>, Derek N. Woolfson<sup>1,8,9,\*</sup>

<sup>1</sup>School of Chemistry, University of Bristol, Cantock's Close, Bristol, BS8 1TS, UK

<sup>2</sup>Present address: Theoretical Molecular Science Laboratory, RIKEN Cluster for Pioneering Research, RIKEN, 2-1 Hirosawa, Wako, Saitama 351-0198, Japan

<sup>3</sup>Department of Pharmaceutical Chemistry, University of California San Francisco, San Francisco, CA 94158, USA

<sup>4</sup>Department of Chemistry, King's College London, Britannia House, 7 Trinity Street, London, SE1 1DB, UK

<sup>5</sup>Department of Chemistry, University of Oxford, Chemistry Research Laboratory, Mansfield Road, Oxford, OX1 3TA, UK

<sup>8</sup>School of Biochemistry, University of Bristol, Medical Sciences Building, University Walk, Bristol, BS8 1TD, UK

<sup>9</sup>Bristol BioDesign Institute, University of Bristol, Life Sciences Building, Tyndall Avenue, Bristol BS8 1TQ, UK

<sup>10</sup>School of Chemical Biology and Biotechnology, Peking University Shenzhen Graduate School, Shenzhen 518055, Peoples Republic of China

<sup>11</sup>DLX Scientific, Lawrence, KS 66049, USA

# These authors contributed equally to this work.

### Abstract

Users may view, print, copy, and download text and data-mine the content in such documents, for the purposes of academic research, subject always to the full Conditions of use: [http://www.nature.com/authors/editorial\\_policies/license.html#terms](http://www.nature.com/authors/editorial_policies/license.html#terms)

\*Corresponding author. [d.n.woolfson@bristol.ac.uk](mailto:d.n.woolfson@bristol.ac.uk).

<sup>6</sup>Present address: Membrane Biology Laboratory, Interdisciplinary Research Program, Rajiv Gandhi Centre for Biotechnology, Thiruvananthapuram, 695014, India.

<sup>7</sup>Present address: School of Chemistry, Joseph Black Building, University Avenue, Glasgow G12 8QQ, UK.

#### Author contributions

A.J.S., A.N., K.R.M., A.R.T. H.B., R.L.B. and D.N.W. conceived the project and designed the peptides, which A.J.S., A.N. and W.M.D. synthesized. A.J.S., A.N. and K.R.M performed solution-phase biophysics and electrophysiology experiments. A.J.S., H.T.K. and L.L. determined X-ray crystal structures. A.J.S. and A.R.T. did the computational design. E.J.M.L., M.M. and A.J.M. ran and analysed the MD simulations. E.J.M.L. conducted the electrostatic calculations. J.T.S. and M.I.W. conducted and analysed the oSCR. A.J.S. and A.N. contributed equally as first authors to this work. The contributions of H.T.K., E.J.M.L. and J.T.S. were also equal. A.J.S., E.J.M.L. and D.N.W. wrote the manuscript, to which all authors contributed.

#### Competing interests

The authors declare no competing interests.

The design of peptides that assemble in membranes to form functional ion channels is challenging. Specifically, hydrophobic interactions must be designed between the peptides and at the peptide-lipid interfaces simultaneously. Here, we take a multi-step approach towards this problem. First, we use rational *de novo* design to generate water-soluble  $\alpha$ -helical barrels with polar interiors, and confirm their structures using high-resolution X-ray crystallography. These  $\alpha$ -helical barrels have water-filled lumens like those of transmembrane channels. Then, we modify the sequences to facilitate their insertion into lipid bilayers. Single-channel electrical recordings and fluorescent imaging of the peptides in membranes show monodisperse, cation-selective channels of unitary conductance. Surprisingly, however, an X-ray structure solved from lipidic cubic phase for one peptide reveals an alternative state with tightly packed helices and a constricted channel. To reconcile these observations, we perform computational analyses to compare the properties of possible different states of the peptide.

---

The *de novo* design of water-soluble proteins has progressed rapidly<sup>1,2</sup>. In comparison, membrane protein design is less developed. Indeed, relatively few *de novo* membrane proteins have been defined in structural detail: helical bundles have been specified by computationally designed hydrogen-bond networks<sup>3</sup> or side-chain packing<sup>4</sup>, and a  $\text{Zn}^{2+}/\text{H}^+$  antiporter has been achieved<sup>5</sup>. Moreover, many natural membrane proteins respond to chemical and physical cues; *e.g.*, G-protein coupled receptors, ligand- and voltage-gated ion channels, and water-soluble toxins that form membrane-spanning pores. The *de novo* design of such multi-state systems is particularly challenging<sup>6,7</sup>.

The self-assembly of *de novo*  $\alpha$ -helical peptides presents an attractive route to address the challenge of designing transmembrane proteins. This is because established structural principles for  $\alpha$ -helical folding and assembly provide starting points for design<sup>2,8</sup>. Nonetheless, there are relatively few successful *de novo* designs of functional transmembrane peptides such as ion channels<sup>9,10</sup>. Advancing the design field to deliver such targets requires solutions to three interlinked design challenges: first, helix-helix interactions must be specified to maintain discrete oligomers; second, this has to be done in competition with interactions needed to interface the structures with lipids; third, the assemblies must have accessible, water-filled lumens lined with polar residues, which may compromise helix-helix packing and structural stability. Moreover, a particular challenge is that this all has to be encoded within approximately 30-residue peptides, the length required for an  $\alpha$  helix to span a lipid bilayer<sup>11,12</sup>.

Here, we combine rational and computational design to produce peptides that self-assemble into water-soluble  $\alpha$ -helical barrels. These have polar lumens wetted by dynamic networks of water molecules. With insights from these structures, we introduce outwardly projecting hydrophobic residues to generate membrane-spanning peptides. These form well-defined ion channels that conduct approximately  $10^8$  ions per second. These are the first examples of modifying water-soluble, self-assembling *de novo* peptides to facilitate membrane insertion. Moreover, in membranes, the peptides form channels with lifetimes unprecedented for designed systems, allowing their dynamics to be imaged directly. We present a crystal structure for one peptide assembly from the lipidic cubic phase. This reveals an unanticipated alternate state with tightly packed helices. This is almost certainly a non-

conducting state. To reconcile these data, we use computational analyses to develop a model for the peptide's structure and activity. We posit that the multiple states observed can be understood in terms of the relative energetics of helix-packing interactions in water-soluble and membrane proteins, and possibly the influence of vectorial insertion of peptides into membranes. This study highlights the challenges of designing discrete membrane-spanning ion channels from self-assembling peptides, which we discuss and place in a wider context.

## Results and discussion

### Water-soluble $\alpha$ -helical barrels with solvated channels can be designed

To start the design process, we targeted  $\alpha$ -helical-barrel ( $\alpha$ HB) coiled-coil peptides. These have 'Type-2' heptad sequence repeats of hydrophobic (h) and polar (p) residues, hpphhph (labelled abcdefg), which assemble into bundles of five or more  $\alpha$  helices<sup>13,14</sup>. Previously, we have developed design principles and methods for water-soluble and membrane-spanning  $\alpha$ HBs<sup>4,15</sup>. These exploit tight interhelical packing of mostly hydrophobic residues to specify the association states and internal radii of the assemblies. This packing stabilizes the structures, but it precludes their use as ion-channels. Therefore, we sought to place polar residues capable of favourable interactions with water into the lumens of  $\alpha$ HBs.

We took a canonical water-soluble  $\alpha$ HB (CC-Hept<sup>15</sup>, systematically named CC-Type2-(L<sub>a</sub>I<sub>d</sub>)<sub>4</sub>), with the following features (Fig. 1a and Table 1): Hydrophobic Leu at position a and Ile at position d point into the lumen but also stabilize interactions between neighbouring helices; small hydrophobic Ala residues at e and g positions supplement the helical interfaces to specify high-order bundles; and interactions between charged Lys and Glu side chains at b and c positions contribute further to the interfaces and provide water solubility. We explored placing neutral polar side chains at the luminal a and d sites in this background (Fig. 1, Table 1, and Supplementary Table 1).

Because  $\beta$ -branched side chains at a and d positions help maintain open barrels<sup>16</sup>, first we explored  $\beta$ -branched and polar Thr residues at these sites. Computational design<sup>17</sup> indicated that Thr at an a position was compatible with the knobs-into-holes (KIH) packing of coiled coils<sup>18</sup> and that the  $\beta$ -hydroxyl group projected into the lumen (Fig. 1b), whereas Thr at d could not assume this arrangement. To test this, we synthesized two peptides with Thr at five consecutive a or d positions, CC-Type2-(T<sub>a</sub>I<sub>d</sub>)<sub>5</sub> and CC-Type2-(L<sub>a</sub>T<sub>d</sub>)<sub>5</sub> (Table 1, and Supplementary Figs. 2,3). We examined their folding and assembly by far-UV circular dichroism (CD) spectroscopy and analytical ultracentrifugation (AUC); and we probed the binding of the environment-sensitive dye 1,6-diphenyl-1,3,5-hexatriene (DPH), which binds to open barrels but not to collapsed bundles<sup>16</sup>. Both peptides formed helical oligomers (Fig. 1c,d, Table 1, and Supplementary Figs. 19,20,32,33), but only CC-Type2-(T<sub>a</sub>I<sub>d</sub>)<sub>5</sub> bound DPH (Supplementary Fig. 38).

We determined a 1.9 Å resolution X-ray crystal structure for CC-Type2-(T<sub>a</sub>I<sub>d</sub>)<sub>5</sub> (Fig. 1e, and Supplementary Table 2), and another for the related CC-Type2-(T<sub>a</sub>I<sub>d</sub>)<sub>2</sub> to 1.2 Å. These revealed parallel hexameric  $\alpha$ HBs with internal Thr and Ile side chains in alternating layers. The hydroxyl groups of Thr stabilize small clusters of water molecules (Supplementary Fig.

40). CC-Type2-(T<sub>a</sub>I<sub>d</sub>)<sub>5</sub> is the first coiled coil with just one large hydrophobic residue per heptad repeat, and with an associated internal water network.

We explored the stability of this water using all-atom molecular dynamics (MD) simulations, analysed with CHAP<sup>19</sup>, starting from a fully hydrated channel (Fig. 1h,i,j). The channel remained solvated through 1.5 μs of simulations (Fig. 1h). Moreover, water molecules exchanged freely between the channel and bulk solvent (Supplementary Figs. 41-51, and Supplementary Movie 1). By comparison, in similar simulations for a hexamer with all Leu at a positions and all Ile at d positions (CC-Hex2, CC-Type2-(L<sub>a</sub>I<sub>d</sub>S<sub>g</sub>)<sub>4</sub>,<sup>15</sup>) the introduced water was immediately expelled from the channel, leaving it predominantly dry (Fig. 1i, Supplementary Figs. 41-51, and Supplementary Movie 2).

Despite the mobility of water in the channel, we anticipated that the Ile layers of CC-Type2-(T<sub>a</sub>I<sub>d</sub>)<sub>5</sub> might present barriers to the passage of hydrated ions.<sup>20</sup> Therefore, we tested other small polar residues at the luminal sites (Supplementary Table 1); *e.g.*, Ser at a and d to give CC-Type2-(S<sub>a</sub>I<sub>d</sub>)<sub>5</sub> and CC-Type2-(L<sub>a</sub>S<sub>d</sub>)<sub>5</sub> (Table 1). The former was unfolded. The latter assembled into a helical oligomer (Fig. 1c,d, Table 1, and Supplementary Figs. 22,34). Thus, Ser residues appear better accommodated at d sites. We could not crystallize CC-Type2-(L<sub>a</sub>S<sub>d</sub>)<sub>5</sub>. Next, we made peptides with Thr and Ser at consecutive a at d sites. A peptide with two such heptads braced by Leu/Ile-based heptads, CC-Type2-(T<sub>a</sub>S<sub>d</sub>)<sub>2</sub>, formed stable helical hexamers in solution (Fig. 1c,d, Table 1). This crystallized as a hexameric αHB (Fig. 1f) with a large cavity (diameter ≈7 Å, length ≈20 Å) occupied by an unusually high number (≈38) of ordered water molecules<sup>21</sup>. To our knowledge, this is the largest such cavity built into a *de novo* protein. The internal water molecules formed an intricate hydrogen-bonded network involving hydroxyl groups of the Ser and Thr side chains and lumen-facing backbone carbonyl groups (Fig. 1g). In MD simulations the hydrated channel was stable, and water freely exchanged in and out of it (Fig. 1j, Supplementary Figs. 41-51, Supplementary Movie 3).

### The water-soluble barrels can be converted into membrane-spanning assemblies

To convert these water-soluble αHBs into transmembrane ion channels, we extended the Thr/Ser-based lumen of CC-Type2-(T<sub>a</sub>S<sub>d</sub>)<sub>2</sub> over a length required to span a membrane and increased the hydrophobicity of the exterior residues. We reasoned that multiple Thr/Ser at the a/d positions might give stable membrane-spanning barrels because these residues promote helix-helix interactions in membranes<sup>22</sup>. In the resulting ‘CCTM’ designs, the Ala residues were retained at the e and g positions, and the exterior f positions were made Trp or Leu to match preferences for locating to headgroup and hydrocarbon regions of lipid bilayers, respectively<sup>23</sup> (Fig. 2a). Initially, the b and c positions were made Leu. This peptide, CCTM-L<sub>b</sub>L<sub>c</sub> (Table 1), had an *N*-terminal tetra-Lys tag and a *C*-terminal hydrophobic residue to promote *C*-terminal insertion into phospholipid bilayers (PLBs)<sup>10</sup>. Encouragingly, CCTM-L<sub>b</sub>L<sub>c</sub> was α helical in *n*-dodecyl β-D-maltoside (DDM) solutions (Fig. 2b and Supplementary Fig. 26).

To test for functional ion channels, we used single-channel electrical recordings across diphytanoyl-*sn*-glycero-3-phosphocholine (DPhPC) PLBs at +100 mV in 1 M KCl. CCTM-L<sub>b</sub>L<sub>c</sub> was added from micellar solutions to the *cis* (ground) side of the bilayer. This diluted

the solutions below their critical micelle concentration. The formation of individual channels was evident from uniform steps in ionic current of  $\approx 12$  pA (Fig. 2c), corresponding to  $\approx 7.5 \times 10^7$  ions/sec. Based on this, conductance histograms (Fig. 2c) confirmed homogeneous channels with a unitary conductance of  $\approx 0.12$  nS.

Using a computational coiled-coil design method<sup>15</sup>, we explored the effect on ion-channel properties of placing different hydrophobic residues at b and c positions to optimize helix-helix packing<sup>4</sup>. The top-scoring sequences had Val/Ile, Ile/Ile and Leu/Ile combinations at the b/c positions (Supplementary Table 3). In single-channel PLB experiments, the peptides with Ile/Ile and Leu/Ile at b/c formed channels that no longer had a single conductance but showed increasingly large steps in current (Fig. 2d). This is reminiscent of alamethicin pores, which increase oligomeric state by sequential additions of peptide<sup>24</sup>. By contrast, channels formed by CCTM-V<sub>b</sub>I<sub>c</sub> (with Val/Ile at b/c; Fig. 2e,f) were monodisperse, longer-lived than for CCTM-L<sub>b</sub>L<sub>c</sub> or foregoing *de novo* peptide channels<sup>9</sup>, and exhibited less gating (Fig. 2, and Supplementary Fig. 52).

All of the CCTM peptides were  $\alpha$  helical in DDM solutions (Supplementary Figs. 26-30). In AUC experiments, the two variants of CCTM-V<sub>b</sub>I<sub>c</sub> (Table 1) clearly associated in detergent solutions (Supplementary Figs. 36,37). However, the sizes of the oligomers formed depended on the variant and the detergent used. In our understanding, AUC of pore-forming peptides with association states larger than four or five is notoriously difficult, and there are no reports of such experiments that reveal the assembly of an active barrel-stave-pore state.

### CCTM-V<sub>b</sub>I<sub>c</sub> forms antiparallel helical bundles in the lipidic cubic phase

Despite the difficulties encountered with AUC, having derived a CCTM design with favourable ion-channel properties we sought to solve its structure. A 2.1 Å resolution X-ray structure was determined for K<sub>2</sub>-CCTM-V<sub>b</sub>I<sub>c</sub> (Table 1) crystallized from the lipidic cubic phase (LCP)<sup>25</sup>. This confirmed a bundle of amphipathic  $\alpha$  helices with Type-2 KIH packing involving most a, d, e and g positions (Fig. 3a,b, and Supplementary Table 4). Surprisingly, however, the structure had two antiparallel 4-helix bundles associated laterally to form an octamer (Fig. 3a,b). While at odds with our target of a parallel  $\alpha$ HB, we sought to reconcile this observation with sequence features of the CCTM-V<sub>b</sub>I<sub>c</sub>.

The CCTM-V<sub>b</sub>I<sub>c</sub> sequence has small Ala and Ser residues each spaced seven residues apart. These are the hallmarks of alanine and serine zippers, which have tightly packed antiparallel helices<sup>26-28</sup>. The observed structure appears to maximise the number of these zippers (Fig. 3c), and it allows the Ser and Thr residues to form an extensive hydrogen-bonded network. However, this leaves space for only a few isolated pairs of water molecules (Fig. 3d). The lack of a more substantial pore hints that this conformation is not the active ion-conducting state of CCTM-V<sub>b</sub>I<sub>c</sub> (see below), but an alternative state accessible on the free-energy landscape for the peptide sequence. Similar antiparallel structures are known. For example, the water-soluble peptide CC-Hex-L24E crystallises as either a parallel 6-helix  $\alpha$ HB or an antiparallel tetramer, depending on conditions<sup>29</sup>. Hence, both structures are accessible to CCTM-V<sub>b</sub>I<sub>c</sub>, and likely close in energy. In addition, the few available X-ray structures of natural membrane-spanning pore-forming  $\alpha$ -helical peptides have antiparallel helices<sup>30-32</sup>, though these are not necessarily the active states<sup>33</sup>.

## CCTM-V<sub>b</sub>I<sub>c</sub> forms well-defined ion-channels in planar-lipid membranes

The apparent contradiction between the crystal structure of K<sub>2</sub>-CCTM-V<sub>b</sub>I<sub>c</sub> and its channel properties in lipid bilayers led us to make further electrical recordings.

Single CCTM-V<sub>b</sub>I<sub>c</sub> channels had a unitary conductance of  $0.15 \pm 0.01$  nS (+100 mV, 1 M KCl, Fig. 2f), corresponding to  $\approx 9 \times 10^7$  ions/sec, a high conductance for synthetic peptide channels<sup>9</sup>. This suggests a channel diameter of  $\approx 10 \text{ \AA}^{34}$ , far closer to that predicted for the water-soluble hexamer, CC-Type2-(T<sub>a</sub>S<sub>d</sub>)<sub>2</sub>, than to the four-helix bundles of the octamer (see below). Reversal potential measurements showed that the channels were cation-selective, with a permeability ratio of  $\approx 5:1$  for K<sup>+</sup> versus Cl<sup>-</sup> (Supplementary Fig. 54), consistent with the solvation of cations by hydroxyl groups of Ser/Thr-lined channels. CCTM-V<sub>b</sub>I<sub>c</sub> also conducted Na<sup>+</sup> and Cs<sup>+</sup>, and current-voltage curves obtained in different electrolytes were non-linear with marked current rectification (Fig. 2g). Such rectification arises from asymmetric charge distributions<sup>35,36</sup>. This is consistent with a parallel assembly of helices with N-terminal Lys tags, but not with the antiparallel arrangement seen in the LCP structure of K<sub>2</sub>-CCTM-V<sub>b</sub>I<sub>c</sub> (see below).

In addition, we performed simultaneous electrical and optical single-channel recording, oSCR<sup>24,37,38</sup>, monitoring the flux of calcium ions through individual CCTM-V<sub>b</sub>I<sub>c</sub> channels inserted into DPhPC droplet-interface bilayers (DIBs; Fig. 4 and Supplementary Figs. 55,56)<sup>39</sup>. Electrically, as in PLBs, CCTM-V<sub>b</sub>I<sub>c</sub> showed discrete unitary conductance in DIBs (Fig. 4b). Optically, the calcium flux imaging showed multiple mobile spots diffusing in the plane of the bilayer, indicative of transmembrane channels (Fig. 4c & Supplementary Movie 4). The fluorescence from these isolated channels showed single distinct open and closed states, further demonstrating the unitary conductance of the CCTM-V<sub>b</sub>I<sub>c</sub> channels (Fig. 4d,e).

Direct imaging of a Cyanine 5-labelled peptide, Cy5-CCTM-V<sub>b</sub>I<sub>c</sub>, showed it diffused across the entire membrane, including regions away from the channels seen by oSCR (Supplementary Fig. 56). These species had a mean lateral diffusion coefficient ( $D_{\text{lat}}$ ) of  $2.56 \pm 0.99 \mu\text{m}^2\text{s}^{-1}$ , similar to monomeric transmembrane helices in related membranes<sup>40</sup>. However, the Ca<sup>2+</sup>-conducting channels diffused more slowly ( $D_{\text{lat}} = 1.05 \pm 0.26 \mu\text{m}^2\text{s}^{-1}$ , similar to multi-peptide alamethicin pores<sup>24</sup>). Using these  $D_{\text{lat}}$  values in the Saffman-Delbrück equation<sup>41</sup>, we estimated an approximate 4-fold increase in diameter between the individual peptides and the conductive channels (Supplementary Fig. 55). Although this carries assumptions, it is consistent with the relative sizes of helical monomers and  $\alpha$ HBs<sup>15</sup>.

## Computational analyses of possible antiparallel and parallel states of CCTM-V<sub>b</sub>I<sub>c</sub>

Finally, to help distinguish between the possible states that CCTM-V<sub>b</sub>I<sub>c</sub> might form in the membrane, we performed simulations and *in silico* calculations on the K<sub>2</sub>-CCTM-V<sub>b</sub>I<sub>c</sub> structure, *i.e.* the dimer of antiparallel 4-helix bundles, and with the peptide modelled as parallel and antiparallel hexamers (Fig. 3e-i). Hexamers were chosen to match the oligomeric state of the water-soluble parent and consistent with the conductance data. The models were generated in CCBuilder2<sup>17</sup> using parameters from CC-Type2-(T<sub>a</sub>S<sub>d</sub>)<sub>2</sub> X-ray crystal structure.



In contrast to simulations for the water-soluble barrels (Fig. 1h,i,j), MD studies of the K<sub>2</sub>-CCTM-V<sub>b</sub>I<sub>c</sub> octamer in DPhPC bilayers indicated that very few water molecules traversed the channel or exchange with bulk solvent (Supplementary Figs. 57-60, and Supplementary Movie 5). Rather, and consistent with the ordered crystallographic water, water molecules remained bound to internal Ser and Thr side chains of the outer four-helix bundles for hundreds of nanoseconds (Supplementary Table 5). In short, these interiors were rarely solvated across their full lengths. Moreover, ions included in different simulations (*e.g.*, Ca<sup>2+</sup>, Na<sup>+</sup>, K<sup>+</sup>, Cl<sup>-</sup>) did not enter these spaces over a cumulative 3.2  $\mu$ s of simulation. *N.B.* The interior of the inner four-helix bundle remained dry in all simulations.

Poisson-Boltzmann electrostatic calculations using APBSmem<sup>42</sup> supported these findings (Fig. 3e, and Supplementary Figs. 61-67): The calculated electrostatic potential energy barriers for the outer four-helix bundle of the octameric crystal structure were too high to conduct K<sup>+</sup> or Cl<sup>-</sup> (Fig. 3f). However, the barriers calculated for the parallel hexameric model were an order of magnitude lower and similar to those calculated for natural ion channels (Fig. 3g)<sup>43</sup>. We attribute this to the different diameters of the cavities in the four- and six-helix models (Fig. 3h). The K<sup>+</sup>/Cl<sup>-</sup> selectivity observed experimentally was manifest in the calculations as a lower energy profile for K<sup>+</sup> compared with Cl<sup>-</sup> for the hexamers (Fig. 3g), which we attribute to the hydroxyl groups lining the channel. Finally, we modelled the current-voltage relationship using Nernst-Planck electrodiffusion theory<sup>34</sup>. The computed I-V curve for the parallel hexameric model agreed qualitatively with the current rectification observed experimentally (Fig. 2g, 3i, and Supplementary Figs. 61-67). By contrast, the calculated I-V plot for the antiparallel hexameric model was linear; and no current was predicted for the octameric crystal structure across the voltage range. From these analyses, we propose an all-parallel barrel-like structure, possibly a hexamer, as the most-likely open-channel state.

## Conclusion

We have shown that multiple polar residues can be incorporated within the lumens of water-soluble, *de novo*  $\alpha$ -helical barrels ( $\alpha$ HBs) with a $\rightarrow$ g heptad-repeat sequences. The combination of Thr at a positions and Ser at d positions generates large cavities that sequester water molecules that freely exchange with bulk water. This background can be used to generate ion-conducting membrane-spanning peptides by introducing hydrophobic residues at the b, c and f positions. One of these CCTM peptides forms discrete and stable ion channels in membranes. Designed peptide channels with this degree of stability and monodispersity are unprecedented and reminiscent of those formed by the engineered natural peptides cWza and pPorA<sup>10,44</sup>. This demonstrates how consideration of helix-helix packing and lumen design can deliver membrane-spanning assemblies with defined ion-channel activities.

That said, the peptides that we have made access multiple states. One of our CCTM peptides crystallizes from the lipidic cubic phase (LCP) as a dimer of an antiparallel tetramer, while in membranes under voltage both monomeric peptides and assembled channels are observed. The antiparallel tetramers are unlikely to be the channel state: although they have polar interiors, these are too narrow to conduct ions, and their dihedral

symmetry is inconsistent with rectification observed for the conducting state. Given this, we propose the following model for CCTM activity, though we recognise that different membrane mimics may result in different assemblies. In the lipidic cubic phase, the antiparallel structure is a low-energy, readily accessible state. By contrast, in planar lipid bilayers the peptide forms an equilibrium of monomeric and oligomeric species. The voltage applied to record channel currents may aid in establishing the channels, either by increasing local peptide concentration or thinning the membrane. However, in DIBs, peptide concentrations of 100 – 350 nM give currents from hundreds of channels even at low voltage (10 – 20 mV), suggesting that channels insert readily. For the conducting state, we propose a parallel  $\alpha$ -helical barrel-stave structure with a solvent-accessible central channel similar to those seen in the water-soluble parent peptides. This multi-state behaviour mimics natural channel-forming peptides, the structures of which are often condition-dependent<sup>33</sup>.

Of course, without a high-resolution structure of the conducting state, we cannot be certain of this model. Given the apparent structural plasticity of the system, it may prove difficult to obtain such a structure. It may be possible to stabilise the active state through templating<sup>45</sup>, or to employ negative design to destabilise the alternate state(s)<sup>46</sup>. However, the generation of stable barrel-stave structures of peptide helices may continue to prove challenging. Indeed, we find that water-soluble  $\alpha$ HBs collapse without key sequence features<sup>16</sup>. We observe something similar in the LCP structure of CCTM, where close packing of the Ala, Ser, Thr core residues leads to the dimer of four-helix bundles. Furthermore, it is interesting that although nature has evolved stable membrane-spanning  $\alpha$ HBs that are crystallisable, these are usually templated by extra-membranous domains or buttressed by concentric rings of helices in the membrane<sup>47,48</sup>. Indeed, recently Xu, Baker and colleagues have successfully built membrane-spanning pores using precisely this strategy.<sup>49</sup> Interestingly, in early iterations of these designs (WSHC6 and TMHC6) an outer ring of helices buttresses a central 6-helix barrel based on the *de novo* designed  $\alpha$ HB CC-Hex2,<sup>15</sup> in which the original barrel-specifying luminal and inter-helical hydrophobic residues are retained. Further still, many natural membrane pores are assembled from multiple  $\beta$ -hairpin units<sup>47,50</sup>. Although extremely large barrels appear to be accessible through this mode of assembly, again they are often templated by large water-soluble domains. Efforts to design even water-soluble  $\beta$ -barrel systems are in their infancy<sup>51</sup>, and carry the added challenge of avoiding amyloid states.

Thus, whilst our work and examples of natural membrane-spanning  $\alpha$ HBs offer hope for designing such assemblies, they do not completely solve the problem of how to specify peptide-peptide interactions to generate barrel-stave structures that are stable over broad conditions. Nonetheless, we have achieved considerable control over self-assembly in water and function in membranes. Improving on this further would increase understanding of natural channel and pore-forming peptides, provide further principles for designing peptide ion channels, and, ultimately, unlock applications for these in biotechnology<sup>50</sup>.

## Methods

Computational modelling and simulation methodology is described in the Supplementary Information file.



## Solid-phase Peptide Synthesis

Fmoc-protected amino acids, synthesis-grade dimethylformamide (DMF) and coupling agents were purchased from Cambridge Reagents (UK). Fmoc-protected pseudoproline dipeptides and MBHA resin were supplied by Novabiochem (Merck Millipore, Germany). Peptides were synthesized on a 0.1 mmol scale using a CEM (Buckingham, UK) Liberty Blue automated peptide synthesizer equipped with inline UV monitoring, and using standard Fmoc-protected amino acid chemistry as previously described<sup>15</sup>. The activators used were *N,N*-diisopropylcarbodiimide (DIC) and 6-chloro-1-hydroxybenzotriazole (Cl-HOBt). Rink amide MBHA resin was used, which after cleavage yielded peptides with a *C*-terminal amide group. Peptides were *N*-terminally acetylated using acetic anhydride and pyridine. For CCTM peptides, Fmoc-Ala-Thr( $\psi^{\text{Me,Me}}\text{pro}$ )-OH was used at all Ala-Thr positions.

## Semi-preparative HPLC

Crude peptides were purified using a Jasco 2000 series HPLC system. Crude peptide solution (1 mL, 6 mg/mL, 20:80% v/v MeCN:H<sub>2</sub>O) was then injected onto a semi-preparative reversed-phase HPLC column and eluted with a 3 mL/min linear gradient of H<sub>2</sub>O:MeCN or H<sub>2</sub>O:IPA over 30 minutes. All HPLC mobile phases were modified with 0.1% TFA. Elution of the peptide was detected with inline UV-monitoring at 220 and 280 nm wavelengths simultaneously.

For water-soluble peptides, a C18 column (Phenomenex Kinetex, 5  $\mu\text{m}$ , 100  $\text{\AA}$ , 10 mm ID x 150 mm L) with a 20-80% or 40-100% MeCN:H<sub>2</sub>O gradient was used. For more hydrophobic peptides, a C8 (Phenomenex Luna, 5  $\mu\text{m}$ , 100  $\text{\AA}$ , 10 mm ID x 250 mm L) or C5 (Phenomenex Luna, 5  $\mu\text{m}$ , 100  $\text{\AA}$ , 10 mm ID x 250 mm L) column was used, often with H<sub>2</sub>O:IPA as the mobile phase. When required, a column oven (50 °C) was employed to improve separation. Pure fractions of peptide, as determined by analytical HPLC and MALDI-TOF MS, were combined and freeze-dried.

## Fluorescent Capping Procedure

To fluorescently label CCTM-V<sub>b</sub>I<sub>c</sub>, the peptide was capped via DIC/Cl-HOBt coupling with 3-(Tritylthio)propionic acid and cleaved/deprotected and purified. To this peptide (0.05  $\mu\text{mol}$ ) in buffer (500  $\mu\text{l}$ , 10% DMF, 10 mM HEPES, pH 6.5) was added tris(2-carboxyethyl)phosphine (TCEP, 1.25 mg, 0.5  $\mu\text{mol}$ ) followed by sulfo-Cyanine5 maleimide (Lumiprobe, DE) in DMSO (0.402 mg, 0.5  $\mu\text{mol}$ , 10 mg ml<sup>-1</sup>). The mixture was rocked overnight at 20 °C, and the dye-labelled peptide purified by reversed-phase HPLC.

## Analytical HPLC

To determine peptide purity (relative to other peptide side products), a small quantity (approx. 10 nmol) of peptide was dissolved in MeCN:H<sub>2</sub>O (20:80 v/v, 50  $\mu\text{L}$ ). This was injected onto an analytical scale C18 column (Phenomenex Kinetex, 5  $\mu\text{m}$ , 100  $\text{\AA}$ , 4.6 mm ID x 100 mm L), and eluted with a linear gradient of 0 – 60%, 20 – 80% or 40 – 100% MeCN:H<sub>2</sub>O with 0.1% TFA, at a flow rate of 1 ml min<sup>-1</sup>. CCTM peptides were injected onto a C4 column (Phenomenex Aeris Widepore) of the same dimensions, and eluted with a 40 – 100% gradient of IPA:MeCN:H<sub>2</sub>O (60:30:10% v/v/v) with 0.1% TFA. Elution of peptide

was monitored at 220 and 280 nm wavelengths simultaneously. All peptides were > 95% pure, as determined by integration of their chromatograms.

### Matrix-Assisted Laser Desorption/Ionization Mass Spectrometry (MALDI-TOF)

MALDI-TOF mass spectra were obtained on a Bruker Ultraflex mass spectrometer, operating in positive-ion reflector mode. Peptides were spotted on a ground steel target plate with either dihydroxybenzoic acid or  $\alpha$ -cyano-4-hydroxycinnamic acid dissolved in MeCN:H<sub>2</sub>O:TFA (49.95:49.95:0.1% v/v/v) as the matrix. The instrument was calibrated by the 'nearest neighbour' method, using Bruker peptide calibration standard II as reference masses.

### Circular Dichroism (CD) Spectroscopy

CD spectra were recorded on either a Jasco J-810 or J-815 spectropolarimeter. Sample temperatures were controlled using a Jasco Peltier thermostatted cell holder. Typically, CD spectra were recorded between 190 and 260 nm wavelength, with a 1 nm interval, 1 nm bandwidth and 1 s response time. A 1 mm pathlength quartz cuvette was used. PBS buffer refers to 8.2 mM sodium phosphate, 1.8 mM potassium phosphate, 137 mM sodium chloride, 2.7 mM potassium chloride.

For thermal denaturation experiments, peptide unfolding and refolding were monitored at 222 nm wavelength. Unless otherwise stated, a temperature range of 5 – 95 °C and a temperature ramp rate of 60 °C per hour were used. Baseline/blank CD spectra were recorded using a buffer and cuvette matched to that of the peptide sample experiment and subtracted from that of the peptide sample. Peptide CD signals are expressed in units of mean residue ellipticity ( $[\theta]$ , deg.cm<sup>2</sup>.dmol<sup>-1</sup>.res<sup>-1</sup>).

### Analytical Ultracentrifugation (AUC)

All AUC experiments were performed using either a Beckman Optima XL-A or XL-I and an An-50 or An-60 Ti rotor. All experiments were conducted at 20 °C. For sedimentation velocity (SV) experiments, a 2-channel epon velocity cell centrepiece equipped with quartz windows was used. The sample channel was filled with 310  $\mu$ L of sample, while the reference channel was filled with 320  $\mu$ L of buffer. Unless otherwise stated, the sample was made to a concentration such that its  $A_{280\text{ nm}}$  (1.2 cm path length) was 1. A typical method involved centrifuging at 50,000 rpm and taking 120 scans, 5.8 to 7.3 cm radially, at 5-minute intervals. A radial calibration was performed prior to every new run. Data for each sample were fitted to a continuous c(s) distribution model using the Sedfit software package, at a 95% confidence level<sup>52</sup>. The buffer density, buffer viscosity and protein partial specific volume were all calculated using the Sednterp package (Biomolecular Interaction Technology Centre). The residuals bitmaps give a visual representation of fit quality. Good fits are uniformly grey without major dark or light streaks.

Sedimentation equilibrium (SE) experiments were conducted using a 6-channel equilibrium cell centrepiece. For absorbance and interference experiments, quartz and sapphire windows were used, respectively. The sample channels were filled with 110  $\mu$ L of sample, and the reference channels filled with 120  $\mu$ L of buffer. Unless otherwise stated, the sample was

made to a concentration such that its  $A_{280\text{ nm}}$  (1.2 cm path length) was 0.5. Where a detergent was used, the micelles and buffer were density matched using  $D_2O$ , in order to remove the detergent's contribution to the peptide-detergent complex buoyant mass. A typical method involved centrifuging from 18 – 36 krpm (in 3000 rpm increments), with scans at 8 and 9 hours after each new speed was reached. A radial calibration was performed prior to every new run. Data were fitted to either a single ideal species model using Ultrascan II (<http://www.ultrascan2.aucsolutions.com/>). If the model was deemed appropriate (as stated in the software fitting report), 95% confidence intervals for the fit were obtained *via* Monte Carlo analysis.

### Crystallography (water-soluble barrels)

Diffraction-quality peptide crystals were grown using a sitting-drop vapour-diffusion method. Freeze-dried peptides were dissolved in ultrapure water, and diluted to 10 mg/ml. Hydrophobic peptides were dissolved in detergent solution. For water-soluble peptides, commercially available sparse matrix screens were used (Morpheus, JCSG plus, Structure Screen 1+2, Pact Premier, ProPlex – Molecular Dimensions Ltd.), and the drops dispensed using a robot (Oryx 8, Douglas Instruments). For each well of an MRC 2-drop plate, 0.3  $\mu\text{L}$  of peptide solution and 0.3  $\mu\text{L}$  of reservoir solution were mixed, and the plate incubated at 20 °C. Crystals generally formed within two weeks, and after looping were soaked in reservoir solution containing 25% glycerol as a cryoprotectant. Diffraction data for the crystals were obtained at the Diamond Light Source (Didcot, UK) on beamlines I03, I04 or I24. For specific wavelengths see Supplementary Table 2.

Diffraction images were processed using either an automated pipeline (xia2, <https://xia2.github.io/>) or manually (iMOSFLM,<sup>53</sup>). In the latter case, data were reduced using POINTLESS<sup>54</sup>, AIMLESS<sup>55</sup> and CTRUNCATE<sup>56</sup>. Data were phased by the molecular replacement method, using Phaser-MR, integrated into the PHENIX software suite<sup>57</sup>. Phasing was achieved using polyalanine search models of the likely structures, with the number of helices present in the asymmetric unit inferred using the Matthews coefficient. CCBUILDER 2.0<sup>17</sup> was used to generate these polyalanine models. Models were refined with phenix.refine and PDB-REDO<sup>58</sup>.

### Crystallography ( $K_2\text{-CCTM-V}_b\text{I}_c$ )

$K_2\text{-CCTM-V}_b\text{I}_c$  was crystallized with the Lipid Cubic Phase (LCP) method. The methods described for LCP crystallization are described in detail in Caffrey and Cherezov<sup>59</sup>. Briefly, lyophilized peptide was weighed and dissolved in ethanol. 60 mg of monoolein (Sigma-Aldrich) was weighed and combined with the peptide solution with vortexing until clear. The solution containing peptide and monoolein was then dried under a stream of  $N_2$  and lyophilized overnight. The LCP was prepared by first heating the monoolein-peptide mixture to 42 °C until it became liquid, and subsequently extruded ~200 times with 2/3 volume of Milli-Q water in coupled gastight Hamilton syringes at room temperature. Successful LCP formation was confirmed as the solution became clear and was not birefringent in the cross-polarizer. The final concentration of the peptide in LCP was estimated to be around 32 mg/mL.

For crystallization, 50 nL of the LCP mixture was dispensed onto 96-well Laminex plastic sandwich plates (Molecular Dimensions) with 1  $\mu$ L of precipitant solution using the TTP Labtech LCP Mosquito robot at room temperature. Plates were sealed using plastic coverslips (Molecular Dimensions) prior to storage and imaging in the Formulatrix RockImager at 20°C. Plates were monitored every day for crystal formation. The initial hit from the sparse matrix screens (0.05 M Glycine pH 9.0, 55% v/v PEG400) was expanded and optimized for the final crystallization condition of 0.05 M Glycine (Sigma-Aldrich) pH 10.0 and 55% v/v PEG400 (Qiagen Sciences).

Crystals were harvested from the crystallization plates and immediately frozen in liquid nitrogen without additional cryoprotection. Crystals were mounted under a cryostream and data was collected at the 8.3.1 beamline at the Advanced Light Source at a wavelength of 1.11582 Å. The data were processed with XDS package<sup>60</sup>, and reduced with AIMLESS<sup>55</sup> in the CCP4 packages. The structure was determined by molecular replacement with ARCIMBOLDO Lite<sup>61</sup>, using a single idea helix as search model. The structure was refined with PHENIX<sup>57</sup>, and model rebuilding was done with Coot<sup>62</sup>. The data processing and structural refinement statistics are listed in Supplementary Table 2.

### 1,6-Diphenyl-1,3,5-hexatriene (DPH) binding assays

Binding experiments with DPH were performed at constant ligand concentrations of 0.1  $\mu$ M or 1  $\mu$ M with 5% v/v DMSO. Peptide concentrations were varied from 1 – 500  $\mu$ M. Datapoints from concentrations corresponding to unfolded peptide were discarded. Samples were equilibrated by rocking for 2 hours at 20 °C. Experiments were conducted using a BMG Labtech (Aylesbury, UK) Clariostar plate reader. Samples were excited at 350 nm wavelength and emission monitored at 455 nm wavelength. Measurements were made in triplicate/quadruplet and averaged to give binding curves, which were analysed using Graphpad Prism 7.

Data were fitted to the following quadratic tight-binding equation:

$$y = B_{\max} \frac{(c_0 + x + K_D) - \sqrt{(c_0 + x + K_D)^2 - 4c_0x}}{2c_0}$$

Where  $y$  is fluorescence intensity,  $x$  peptide concentration,  $B_{\max}$  the fitted maximum fluorescence value and  $c_0$  the ligand (DPH) concentration.

### Planar Lipid Bilayer (PLB) Recordings

PLB single-channel recordings were made using a custom Delrin chamber, with two 1 mL compartments separated by a 20  $\mu$ m thick Teflon film (Goodfellow, UK) with a  $\sim$  80  $\mu$ m diameter aperture<sup>63</sup>. Electrical signals were recorded using a Molecular Devices (USA) Axopatch 200B amplifier, equipped with a CV 203BU headstage. The chamber and headstage were placed in a Faraday cage. Signals were digitized using a Molecular Devices Digidata 1550 digitizer and recorded using the pCLAMP 10.7 software. Data were analysed and plotted using Clampfit 10 and custom Python scripts.

The procedure outlined is based on the Montal-Mueller method of forming folded lipid bilayers<sup>64</sup>. The aperture was pre-painted on both sides with hexadecane in *n*-pentane (3  $\mu\text{L}$ , 10  $\text{mg mL}^{-1}$ ) using a glass micropipette. The pentane was allowed to dry for 15 mins, and the *cis* and *trans* compartments filled with buffer solution (typically 10 mM Tris-HCl, 1 M KCl, pH 8). A drop of 1,2-diphytanoyl-*sn*-glycero-3-phosphocholine (DPhPC) in *n*-pentane ( $\sim 6 \mu\text{L}$ , 5  $\text{mg mL}^{-1}$ ) was added to the buffer surfaces on both sides, and the pentane allowed to evaporate for 15 mins. After this time, buffer solution was removed slowly such that the meniscus fell below the aperture and was gently re-added. This was repeated on both sides of the aperture until a bilayer of the appropriate capacitance had formed. Peptides were added (2  $\mu\text{L}$ , 25  $\mu\text{M}$ , solubilised in 0.05% DDM) to the *cis* compartment to give a final concentration of approximately 50 nM. Voltages were applied between the *cis* (ground) and *trans* (active) compartments using Ag/AgCl electrodes connected to each compartment with salt bridges (3 M KCl, 2% agar). Ag/AgCl electrodes were prepared by leaving Ag wire in sodium hypochlorite solution (5%) overnight.

Reversal potentials (Supplementary **Error! Reference source not found.**) were calculated using asymmetric *cis/trans* electrolytes and a rearranged Goldman-Hodgkin-Katz equation, as described previously<sup>65</sup>.

### Droplet interface bilayer (DIB) electrical and optical recordings

1,2-diphytanoyl-*sn*-glycero-3-phosphocholine (DPhPC) was purchased from Avanti Polar Lipids.  $\text{Ca}^{2+}$ -sensitive dye Fluo-8H was purchased from AAT Bioquest (California, USA). All aqueous solutions were made using ultrapure water.

DIBs were prepared as described previously<sup>39</sup>. Briefly, 0.75% (wt/vol) ultra-low gelling temperature agarose solution was homogenised at 90 °C, and 140  $\mu\text{L}$  of this substrate agarose was spun onto a plasma-cleaned coverslip (Menzel-Gläzer, ThermoFisher Scientific). The coverslip was affixed to the underside of a custom-made poly(methyl methacrylate) device featuring 16 wells, 1 mm in diameter. 1.3% (wt/vol) agarose solution containing 1 M KCl (or 500 mM  $\text{CaCl}_2$  for oSCR experiments), buffered with 10 mM Tris-HCl at pH 8 was flowed into the device, where it made contact with and hydrated the substrate agarose, but did not cover it. The wells were filled with hexadecane containing DPhPC at 10  $\text{mg/mL}$  and the device allowed to rest for 1 hour to allow for monolayer formation on the substrate. Meanwhile, aqueous droplets ( $\sim 100 \text{ nL}$ ) were incubated in the same lipid-in-oil solution, again for monolayer formation. The droplets contained 1 M KCl, 10 mM Tris-HCl, 375  $\mu\text{M}$  EDTA and 46  $\mu\text{M}$  Fluo-8H, in addition to unlabelled (20-100 nM) and N-terminally-labelled CCTM- $\text{V}_b\text{I}_c$  ( $\sim 50$ -100 pM) as required. After incubation, droplets were pipetted into the wells of the device where they sank onto the substrate, forming bilayers by the contact of the droplet and agarose-associated monolayers.

Ag/AgCl electrodes inserted into the hydrating agarose, and the top of the droplet via a micromanipulator, allowed electrical access. Voltages were applied and bilayer currents recorded using an Axopatch 200B patch-clamp amplifier and headstage (Axon Instruments, Molecular Devices, California, USA), with signals recorded and filtered at 1 kHz. Devices were placed within a Faraday cage atop an inverted microscope (TiE Eclipse, Nikon, UK). Fluorescence imaging was carried out using a 60x TIRF objective lens (oil-immersion, 1.45

NA; Nikon). Excitation of the bilayers and collection of fluorescent signals was carried out by the same lens. For excitation of Ca<sup>2+</sup>-bound Fluo-8H, a 473 nm continuous wave laser beam was used (power at the back focal plane of the objective was 40-80  $\mu$ W; Vortran Laser Technology, Sacramento, California, USA), with fluorescence and excitation signals ( $\lambda_{\text{Fluo-8H emission max.}} = 514$  nm) separated by a dichroic mirror (ZT 488/640; Chroma, Vermont, USA), and the collected signal from the bilayer transmitted through an emission filter (Brightline bandpass 550/88 nm; Semrock, Rochester, New York, USA) in order to eliminate stray excitation wavelengths. Cy5-CCTM-V<sub>b</sub>I<sub>c</sub> was excited using a 644 nm continuous wave laser beam (power at the back focal plane of the objective was 450-840  $\mu$ W; Vortran Laser Technology), with the emitted fluorescence passing through a 690/50 nm bandpass emission filter (Semrock). Images were recorded at 31-50 Hz using an electron-multiplying charged-coupled device (EMCCD) camera (iXon+; Andor Technology, Belfast, UK). All experiments were conducted at room temperature of around 21 °C.

### DIB data processing and analysis

Electrical data was recorded using WinEDR electrophysiology software (John Dempster, Strathclyde University, UK). Image analyses were carried out in Fiji image-processing software<sup>66</sup>; single-particle tracking was performed using the TrackMate plugin, using its Laplacian of Gaussian algorithm<sup>67</sup>. Numerical data and MSD vs.  $t$  analyses were performed in Igor Pro (Wavemetrics, Oregon, USA) using custom-written procedures.

Using the measured  $D_{\text{lat}}$  values and Saffman-Delbruck equation<sup>68</sup>, we estimated the ratio of the sizes of the assembled channels versus the monomer,  $r_{\text{channel}}/r_{\text{monomer}}$ , as  $3.9 \pm 1.3$ . This consistent with the relative cross-sections of monomeric  $\alpha$ -helices and hexameric  $\alpha$ -helical barrels, which are  $\approx 1:3$ <sup>15</sup>. This makes the assumption that the monomers are folded as single-pass transmembrane helices (diameter  $\approx 1$  nm), which may not be the case. In addition, we recognize that  $\alpha$ -helical barrels with 5, 6 and 7 helices have similar diameters in the range 3 – 3.5 nm.

For this estimation of  $r_{\text{channel}}/r_{\text{monomer}}$ , the following values were used: membrane thickness,  $h = 3.63$  nm<sup>69</sup>; membrane viscosity,  $\mu_{\text{m}} = 0.08$  Pa.s<sup>68</sup>; surrounding fluid viscosity,  $\mu_{\text{f}} = 1$  mPa.s<sup>68</sup>; temperature,  $T = 294$  K,  $D_{\text{lat, channel}} = 1.05$   $\mu\text{m}^2/\text{s}$ ;  $D_{\text{lat, monomer}} = 2.56$   $\mu\text{m}^2/\text{s}$ .

Values for the membrane viscosity vary in the literature; the value of  $\mu_{\text{m}} = 0.08$  Pa.s was chosen as one that has been shown to produce good agreement between experimentally measured diffusion coefficients and the Saffman-Delbruck model<sup>68</sup>, and is close to the value of 0.1 Pa.s often quoted in the literature.

The error in  $r_{\text{channel}}/r_{\text{monomer}}$  was determined by the propagation of errors, assuming that the only contributions were from  $D_{\text{lat, channel}}$ ,  $D_{\text{lat, monomer}}$  and  $\mu_{\text{m}}$ , the other parameters in the Saffman-Delbrück equation being constant. Whilst not measured in our experiments,  $\mu_{\text{m}}$  was included as a variable in the propagation of errors because a range of values are reported in the literature. The error values for each parameter (which were then used to compute the *total* error by the propagation of errors) were the standard errors (standard deviation/  $n$ ) of the lateral diffusion coefficients (0.0176 and 0.0612  $\mu\text{m}^2/\text{s}$  for the pore and monomer



respectively), and for the error in  $\mu_m$  a value of 0.02 Pa.s was chosen, as it has been shown that the Saffman-Delbrück model applies in the range of  $\mu_m = 0.08 \pm 0.02$  Pa.s for a bilayer of similar thickness<sup>68</sup>. Furthermore,  $\mu_m = 0.08 \pm 0.02$  Pa.s covers the range of membrane viscosities often used in the literature.

## Supplementary Material

Refer to Web version on PubMed Central for supplementary material.

## Acknowledgements

A.J.S. thanks Diamond Light Source for a place on the CCP4 Data Collection and Structure Solution Workshop 2017. E.J.M.L. thanks Shanlin Rao and Gianni Klesse (University of Oxford) for support with CHAP and Frank Marcoline (UCSF) for support with APBSmem. A.J.S. was funded by the Bristol Chemical Synthesis Centre for Doctoral Training funded by the EPSRC (EP/G036764/1). A.N. and K.R.M. were supported by a BBSRC grant to R.L.B., H.B. and D.N.W (BB/J009784/1). W.M.D., A.N., A.J.S., A.R.T. and D.N.W. were funded by ERC Grants to D.N.W. (340764 and 787173). E.J.M.L. was in the BBSRC/EPSC-funded Synthetic Biology Research Centre, BrisSynBio ((BB/L01386X/1). M.I.W. was funded by the BBSRC (BB/R001790/1). W.F.D. was supported by NIH (R35 GM122603), NSF (1709506), US Air Force (1709506) grants. H.T.K. was supported by the NIH Ruth L. Kirschstein NRSA Postdoctoral Fellowship (F32 GM125217). M.M. is supported by the Howard Hughes Medical Institute Gilliam Fellowship. D.N.W. held a Royal Society Wolfson Research Merit Award (WM140008). Beamline 8.3.1 at the Advanced Light Source is operated by the University of California Office of the President, Multicampus Research Programs and Initiatives grant MR-15-328599, the National Institutes of Health (R01 GM124149 and P30 GM124169), Plexxikon Inc. and the Integrated Diffraction Analysis Technologies program of the US Department of Energy Office of Biological and Environmental Research. The Advanced Light Source (Berkeley, CA) is a national user facility operated by Lawrence Berkeley National Laboratory on behalf of the US Department of Energy under contract number DE-AC02-05CH11231, Office of Basic Energy Sciences.

## Data availability statement

X-ray crystal structures have been submitted to the RCSB Protein Data Bank with accession codes 6YAZ, 6YB0, 6YB1, and 6YB2. Data supporting the results and conclusions are available within this paper and the Supplementary Information. Additional raw data are available at Figshare, [https://figshare.com/collections/\\_/5248086](https://figshare.com/collections/_/5248086).

## References

- Huang PS, Boyken SE, Baker D. The coming of age of de novo protein design. *Nature*. 2016; 537:320–327. [PubMed: 27629638]
- Korendovych IV, DeGrado WF. De novo protein design, a retrospective. *Q Rev Biophys*. 2020; 53:e3. [PubMed: 32041676]
- Lu PL, et al. Accurate computational design of multipass transmembrane proteins. *Science*. 2018; 359:1042–1046. [PubMed: 29496880]
- Mravic M, et al. Packing of apolar side chains enables accurate design of highly stable membrane proteins. *Science*. 2019; 363:1418–1423. [PubMed: 30923216]
- Joh NH, et al. De novo design of a transmembrane Zn<sup>2+</sup>-transporting four-helix bundle. *Science*. 2014; 346:1520–1524. [PubMed: 25525248]
- Davey JA, Damry AM, Goto NK, Chica RA. Rational design of proteins that exchange on functional timescales. *Nat Chem Biol*. 2017; 13:1280–1285. [PubMed: 29058725]
- Chen K-YM, Keri D, Barth P. Computational design of G Protein-Coupled Receptor allosteric signal transductions. *Nat Chem Biol*. 2020; 16:77–86. [PubMed: 31792443]
- Woolfson DN. Coiled-Coil Design: Updated and Upgraded. *Subcell Biochem*. 2017; 82:35–61. [PubMed: 28101858]

9. Lear JD, Wasserman ZR, Degrado WF. Synthetic Amphiphilic Peptide Models for Protein Ion Channels. *Science*. 1988; 240:1177–1181. [PubMed: 2453923]
10. Mahendran KR, et al. A monodisperse transmembrane alpha-helical peptide barrel. *Nat Chem*. 2017; 9:411–419. [PubMed: 28430192]
11. Bowie JU. Helix packing in membrane proteins. *J Mol Biol*. 1997; 272:780–789. [PubMed: 9368657]
12. Hong H. Toward understanding driving forces in membrane protein folding. *Arch Biochem Biophys*. 2014; 564:297–313. [PubMed: 25107533]
13. Liu J, et al. A seven-helix coiled coil. *Proc Natl Acad Sci USA*. 2006; 103:15457–15462. [PubMed: 17030805]
14. Zaccai NR, et al. A de novo peptide hexamer with a mutable channel. *Nat Chem Biol*. 2011; 7:935–941. [PubMed: 22037471]
15. Thomson AR, et al. Computational design of water-soluble alpha-helical barrels. *Science*. 2014; 346:485–488. [PubMed: 25342807]
16. Rhys GG, et al. Maintaining and breaking symmetry in homomeric coiled-coil assemblies. *Nat Commun*. 2018; 9(4132)
17. Wood CW, Woolfson DN. CCBUILDER 2.0: Powerful and accessible coiled-coil modeling. *Protein Sci*. 2018; 27:103–111. [PubMed: 28836317]
18. Walshaw J, Woolfson DN. SOCKET: A program for identifying and analysing coiled-coil motifs within protein structures. *J Mol Biol*. 2001; 307:1427–1450. [PubMed: 11292353]
19. Klesse G, Rao SL, Sansom MSP, Tucker SJ. CHAP: A Versatile Tool for the Structural and Functional Annotation of Ion Channel Pores. *J Mol Biol*. 2019; 431:3353–3365. [PubMed: 31220459]
20. Aryal P, Sansom MSP, Tucker SJ. Hydrophobic Gating in Ion Channels. *J Mol Biol*. 2015; 427:121–130. [PubMed: 25106689]
21. Carugo O. Statistical survey of the buried waters in the Protein Data Bank. *Amino Acids*. 2016; 48:193–202. [PubMed: 26315961]
22. Dawson JP, Weinger JS, Engelman DM. Motifs of serine and threonine can drive association of transmembrane helices. *J Mol Biol*. 2002; 316:799–805. [PubMed: 11866532]
23. Hessa T, et al. Molecular code for transmembrane-helix recognition by the Sec61 translocon. *Nature*. 2007; 450:1026–1030. [PubMed: 18075582]
24. Harriss LM, Cronin B, Thompson JR, Wallace MI. Imaging Multiple Conductance States in an Alamethicin Pore. *J Am Chem Soc*. 2011; 133:14507–14509. [PubMed: 21848341]
25. Landau EM, Rosenbusch JP. Lipidic cubic phases: A novel concept for the crystallization of membrane proteins. *Proc Natl Acad Sci USA*. 1996; 93:14532–14535. [PubMed: 8962086]
26. Gernert KM, Surles MC, Labean TH, Richardson JS, Richardson DC. The Alacoil - a Very Tight, Antiparallel Coiled-Coil of Helices. *Protein Sci*. 1995; 4:2252–2260. [PubMed: 8563621]
27. Adamian L, Liang J. Interhelical hydrogen bonds and spatial motifs in membrane proteins: Polar clamps and serine zippers. *Proteins*. 2002; 47:209–218. [PubMed: 11933067]
28. Zhang SQ, et al. The Membrane- and Soluble-Protein Helix-Helix Interactome: Similar Geometry via Different Interactions. *Structure*. 2015; 23:527–541. [PubMed: 25703378]
29. Rhys GG, et al. Navigating the Structural Landscape of De Novo alpha-Helical Bundles. *J Am Chem Soc*. 2019; 141:8787–8797. [PubMed: 31066556]
30. Song C, et al. Crystal structure and functional mechanism of a human antimicrobial membrane channel. *Proc Natl Acad Sci USA*. 2013; 110
31. Hayouka Z, et al. Quasiracemate Crystal Structures of Magainin 2 Derivatives Support the Functional Significance of the Phenylalanine Zipper Motif. *J Am Chem Soc*. 2015; 137:11884–11887. [PubMed: 26369301]
32. Kurgan KW, et al. Retention of Native Quaternary Structure in Racemic Melittin Crystals. *J Am Chem Soc*. 2019; 141:7704–7708. [PubMed: 31059253]
33. Sansom MS. The biophysics of peptide models of ion channels. *Prog Biophys Mol Bio*. 1991; 55:139–235. [PubMed: 1715999]
34. Hille, B. *Ionic Channels of Excitable Membranes*. Oxford University Press; 2001.

35. Kienker PK, DeGrado WF, Lear JD. A helical-dipole model describes the single-channel current rectification of an uncharged peptide ion channel. *Proc Natl Acad Sci USA*. 1994; 91:4859–4863. [PubMed: 7515180]
36. Noskov SY, Im W, Roux B. Ion Permeation through the  $\alpha$ -Hemolysin Channel: Theoretical Studies Based on Brownian Dynamics and Poisson-Nernst-Planck Electrodiffusion Theory. *Biophys J*. 2004; 87:2299–2309. [PubMed: 15454431]
37. Wang SQ, Song LS, Lakatta EG, Cheng HP.  $\text{Ca}^{2+}$  signalling between single L-type  $\text{Ca}^{2+}$  channels and ryanodine receptors in heart cells. *Nature*. 2001; 410:592–596. [PubMed: 11279498]
38. Heron AJ, Thompson JR, Cronin B, Bayley H, Wallace MI. Simultaneous Measurement of Ionic Current and Fluorescence from Single Protein Pores. *J Am Chem Soc*. 2009; 131:1652. [PubMed: 19146373]
39. Leptihn S, et al. Constructing droplet interface bilayers from the contact of aqueous droplets in oil. *Nat Protoc*. 2013; 8:1048–1057. [PubMed: 23640169]
40. Ramadurai S, Duurkens R, Krasnikov VV, Poolman B. Lateral Diffusion of Membrane Proteins: Consequences of Hydrophobic Mismatch and Lipid Composition. *Biophys J*. 2010; 99:1482–1489. [PubMed: 20816060]
41. Saffman PG, Delbrück M. Brownian Motion in Biological Membranes. *Proc Natl Acad Sci USA*. 1975; 72:3111–3113. [PubMed: 1059096]
42. Callenberg KM, et al. APBSmem: A Graphical Interface for Electrostatic Calculations at the Membrane. *Plos One*. 2010; 5:e12722. [PubMed: 20949122]
43. Roux B, Allen T, Berneche S, Im W. Theoretical and computational models of biological ion channels. *Q Rev Biophys*. 2004; 37:15–103. [PubMed: 17390604]
44. Krishnan RS, et al. Autonomously Assembled Synthetic Transmembrane Peptide Pore. *J Am Chem Soc*. 2019; 141:2949–2959. [PubMed: 30702873]
45. Spruijt E, Tusk SE, Bayley H. DNA scaffolds support stable and uniform peptide nanopores. *Nat Nanotechnol*. 2018; 13:739–745. [PubMed: 29808001]
46. Grigoryan G, Reinke AW, Keating AE. Design of protein-interaction specificity gives selective bZIP-binding peptides. *Nature*. 2009; 458:859–864. [PubMed: 19370028]
47. Peraro MD, van der Goot FG. Pore-forming toxins: ancient, but never really out of fashion. *Nature Reviews Microbiology*. 2016; 14:77–92. [PubMed: 26639780]
48. Niitsu A, Heal JW, Fauland K, Thomson AR, Woolfson DN. Membrane-spanning alpha-helical barrels as tractable protein-design targets. *Philos Trans Royal Soc B*. 2017; 372
49. Xu C, et al. Computational design of transmembrane pores. *Nature*. 2020; 585:129–134. [PubMed: 32848250]
50. Howorka S. Building membrane nanopores. *Nat Nanotechnol*. 2017; 12:619–630. [PubMed: 28681859]
51. Dou JY, et al. De novo design of a fluorescence-activating beta-barrel. *Nature*. 2018; 561:485–491. [PubMed: 30209393]
52. Schuck P. Size-distribution analysis of macromolecules by sedimentation velocity ultracentrifugation and Lamm equation modeling. *Biophys J*. 2000; 78:1606–1619. [PubMed: 10692345]
53. Batty TGG, Kontogiannis L, Johnson O, Powell HR, Leslie AGW. iMOSFLM: a new graphical interface for diffraction-image processing with MOSFLM. *Acta Crystallogr D*. 2011; 67:271–281. [PubMed: 21460445]
54. Evans P. Scaling and assessment of data quality. *Acta Crystallogr D*. 2006; 62:72–82. [PubMed: 16369096]
55. Evans PR, Murshudov GN. How good are my data and what is the resolution? *Acta Crystallogr D*. 2013; 69:1204–1214. [PubMed: 23793146]
56. Evans PR. An introduction to data reduction: space-group determination, scaling and intensity statistics. *Acta Crystallogr D*. 2011; 67:282–292. [PubMed: 21460446]
57. Liebschner D, et al. Macromolecular structure determination using X-rays, neutrons and electrons: recent developments in Phenix. *Acta Crystallogr D*. 2019; 75:861–877.

58. Joosten RP, Long F, Murshudov GN, Perrakis A. The PDB\_REDO server for macromolecular structure model optimization. *IUCrJ*. 2014; 1:213–220.
59. Caffrey M, Cherezov V. Crystallizing membrane proteins using lipidic mesophases. *Nat Protoc*. 2009; 4:706–731. [PubMed: 19390528]
60. Kabsch, WXds. *Acta Crystallogr D*. 2010; 66:125–132. [PubMed: 20124692]
61. Sammito M, et al. ARCIMBOLDO\_LITE: single-workstation implementation and use. *Acta Crystallogr D*. 2015; 71:1921–1930. [PubMed: 26327382]
62. Emsley P, Lohkamp B, Scott WG, Cowtan K. Features and development of Coot. *Acta Crystallogr D*. 2010; 66:486–501. [PubMed: 20383002]
63. Maglia G, Heron AJ, Stoddart D, Japrun D, Bayley H. Analysis of Single Nucleic Acid Molecules with Protein Nanopores. *Method Enzymol*. 2010; 475:591–623.
64. Montal M, Mueller P. Formation of Bimolecular Membranes from Lipid Monolayers and a Study of Their Electrical Properties. *Proc Natl Acad Sci USA*. 1972; 69:3561–3566. [PubMed: 4509315]
65. Gu LQ, et al. Reversal of charge selectivity in transmembrane protein pores by using noncovalent molecular adapters. *Proc Natl Acad Sci USA*. 2000; 97:3959–3964. [PubMed: 10760267]
66. Schindelin J, et al. Fiji: an open-source platform for biological-image analysis. *Nat Methods*. 2012; 9:676–682. [PubMed: 22743772]
67. Tinevez JY, et al. TrackMate: An open and extensible platform for single-particle tracking. *Methods*. 2017; 115:80–90. [PubMed: 27713081]
68. Ramadurai S, et al. Lateral Diffusion of Membrane Proteins. *J Am Chem Soc*. 2009; 131:12650–12656. [PubMed: 19673517]
69. Ku erka N, Nieh M-P, Katsaras J. Fluid phase lipid areas and bilayer thicknesses of commonly used phosphatidylcholines as a function of temperature. *Biochim Biophys Acta, Biomembranes*. 2011; 1808:2761–2771.

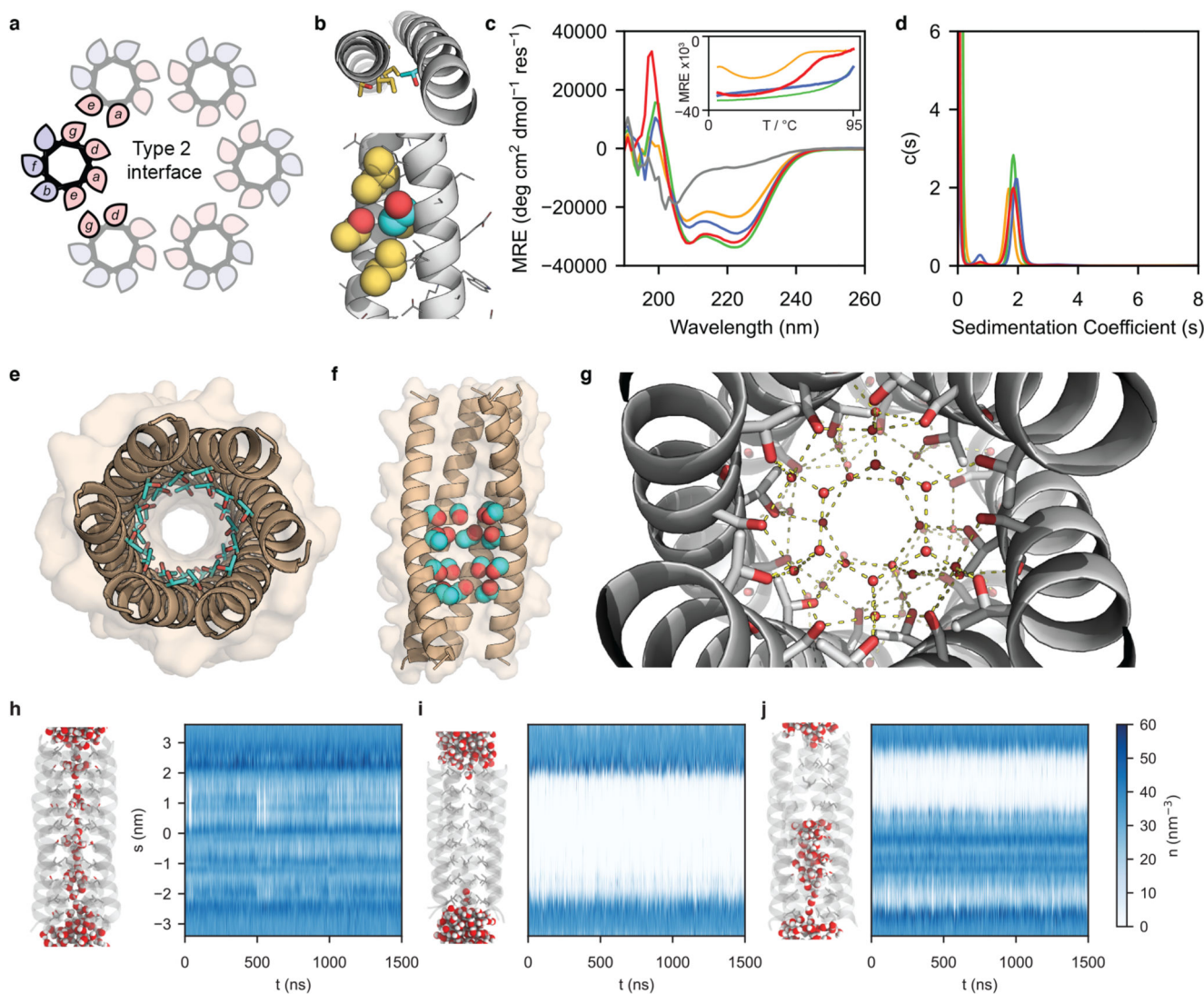


**Fig. 1. Computational design and characterisation of water-soluble  $\alpha$ HBs with solvated lumens.** **a**, Helical wheels for parallel Type-2 coiled-coil interfaces with hydrophobic and polar residues shaded pink and blue, respectively. **b**, CCBuilder2 model of CC-Type2-(L<sub>a</sub>I<sub>d</sub>)<sub>4</sub> with Thr residues at one *a* site. Backbone parameters were from CC-Type2-(L<sub>a</sub>I<sub>d</sub>)<sub>4</sub> (PDB code: 4PNA). Knob and holes residues are coloured cyan and gold, respectively. **c**, CD spectra at 20 °C and thermal denaturation profiles (inset) and **(d)** sedimentation velocity AUC *c*(s) distributions for CC-Type2-(T<sub>a</sub>I<sub>d</sub>)<sub>5</sub> (orange), CC-Type2-(L<sub>a</sub>T<sub>d</sub>)<sub>5</sub> (green), CC-Type2-(S<sub>a</sub>I<sub>d</sub>)<sub>5</sub> (gray), CC-Type2-(L<sub>a</sub>S<sub>d</sub>)<sub>5</sub> (blue), CC-Type2-(T<sub>a</sub>S<sub>d</sub>)<sub>2</sub> (red). **e**, 1.9 Å X-ray crystal structure of CC-Type2-(T<sub>a</sub>I<sub>d</sub>)<sub>5</sub> with internal Thr side chains (cyan) shown as sticks with hydroxyls (red) highlighted. **f**, 1.9 Å X-ray crystal structure of CC-Type2-(T<sub>a</sub>S<sub>d</sub>)<sub>2</sub> with Thr and Ser side chains space-filled, and front two helices removed. **g**, Hydrogen-bonding water (red spheres) network in the lumen of the crystal structure of CC-Type2-(T<sub>a</sub>S<sub>d</sub>)<sub>2</sub>; hydrogen bonds (yellow dashes) are for O-O distances < 3 Å. **h – j**, Molecular dynamics of water ingress into the cavities of CC-Type2-(T<sub>a</sub>I<sub>d</sub>)<sub>5</sub> (**h**), CC-Type2-(L<sub>a</sub>I<sub>d</sub>S<sub>g</sub>)<sub>4</sub> (**i**) and CC-Type2-(T<sub>a</sub>S<sub>d</sub>)<sub>2</sub> (**j**). Left-hand sides: representative snapshots after equilibration, with water molecules space filled

and the *N*termini of the helices at the top. Plots: water number density ( $n$ ) profiles for the channels generated using CHAP.



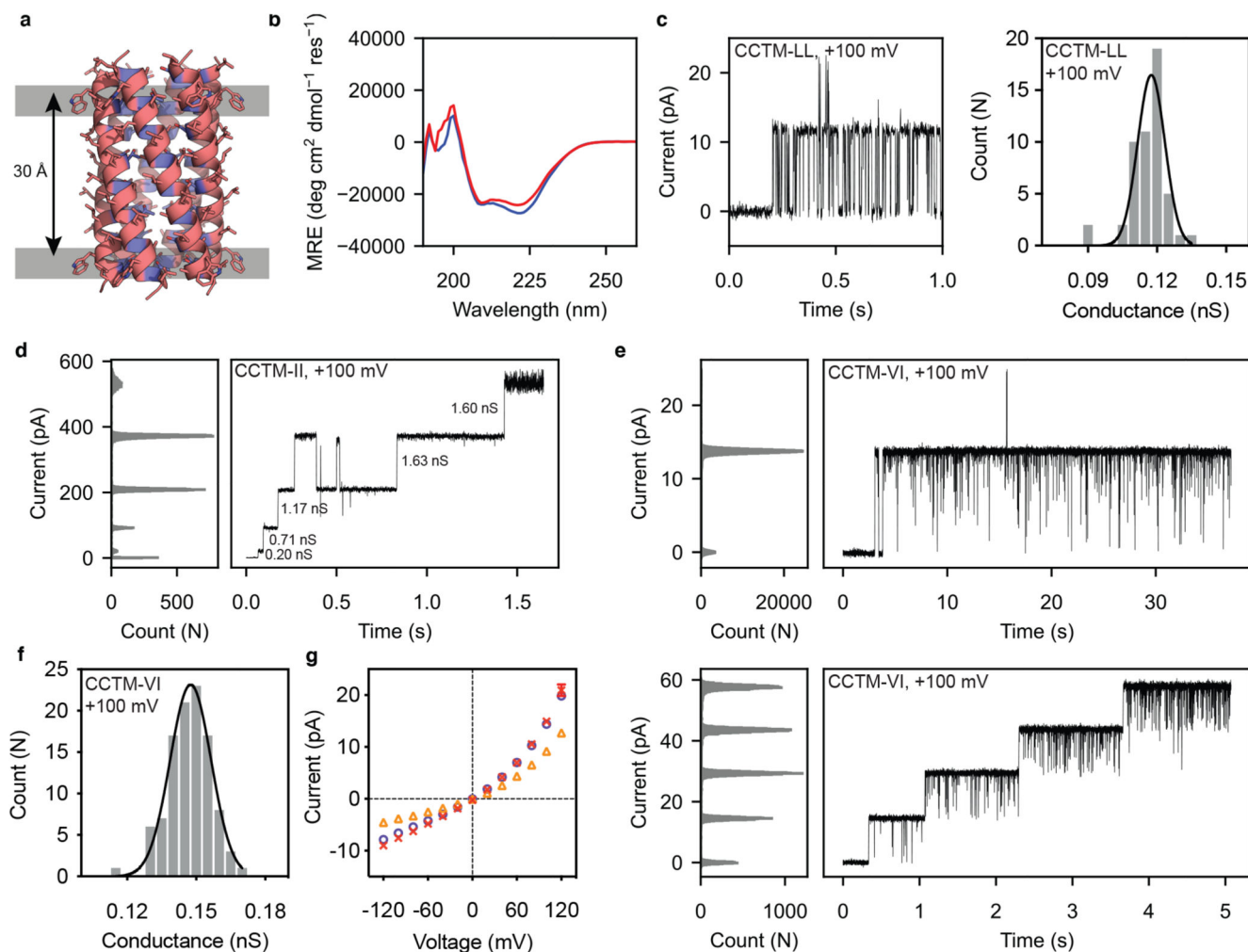


**Fig. 2. Engineering and characterization of transmembrane ion-channel peptides.**

**a**, CC-Builder2 model of CCTM-L<sub>b</sub>L<sub>c</sub> with hydrophobic (Trp, Leu, Ala) and polar (Thr, Ser) residues coloured pink and blue, respectively. The Trp-Trp Ca distance is shown. **b**, CD spectra in 0.05% DDM at 20 °C for CCTM-L<sub>b</sub>L<sub>c</sub> (blue) and CCTM-V<sub>b</sub>I<sub>c</sub> (red). **c**, Insertion of CCTM-L<sub>b</sub>L<sub>c</sub> into a DPhPC PLB (left) and frequency distributions (right) with fitted Gaussian for this conductance ( $n = 51$ ,  $\mu = 0.12$  nS,  $\sigma = 0.01$  nS) at +100 mV potential in 1 M KCl. **d**, CCTM-I<sub>b</sub>I<sub>c</sub> channels recorded at +100 mV in 1M KCl, with the conductance values of different events labelled. **e**, Single (top) and quadruple insertions (bottom) of CCTM-V<sub>b</sub>I<sub>c</sub> at +100 mV. **f**, Frequency distribution histogram for CCTM-V<sub>b</sub>I<sub>c</sub> channels ( $n = 104$ ,  $\mu = 0.15$  nS,  $\sigma = 0.01$  nS) at +100 mV in 1 M KCl. **g**, Current-voltage curves for single CCTM-V<sub>b</sub>I<sub>c</sub> channels. Electrolyte: 1 M each of KCl (purple), NaCl (orange) or CsCl (red). Buffer: 10 mM Tris-HCl, pH 8.0. For all experiments, peptide concentrations in the *cis* compartment were 50 nM, and signals were acquired at 10 kHz and low-pass filtered at 2 kHz.

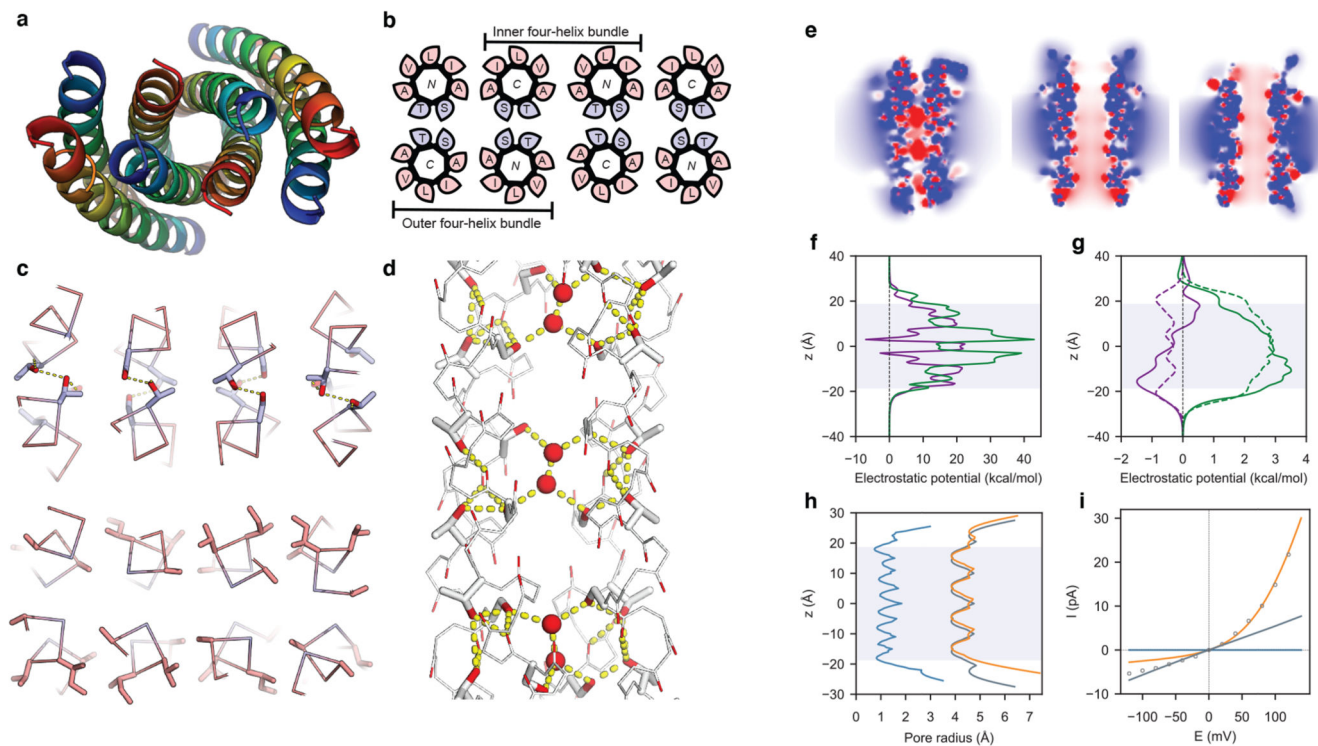


**Fig. 3. LCP crystal structure of  $K_2$ -CCTM- $V_bI_c$  and modelling of alternate states.**

*N.B.* This structure is of a variant with a Lys<sub>2</sub> rather than a Lys<sub>4</sub> *N*-terminal tag; both peptides had similar biophysical and conductance properties (Supplementary Fig. 53). **a**, Axial view of the octameric assembly. *N* to *C* termini are coloured from blue to red. **b**, Corresponding helical wheels showing two distinct four-helix bundles. The inner bundle has a hydrophobic interior of methyl groups from Ala and Thr; whereas, the outer bundles are hydrophilic, lined with hydroxyl groups of Ser and Thr. Blue and pink represent polar and apolar residues, respectively. **c**, A hydrogen-bonded layer of Thr/Ser (blue) at *a/d* (top) and the same layer showing the hydrophobic interfaces with Ala at *e* and *g*, and Val/Ile (pink) at *b/c* (bottom). Hydroxyl groups are shaded red. **d**, Hydrogen-bonding network within the outer bundle involving isolated water molecules (red spheres), Thr/Ser side chains, and backbone carbonyls. Hydrogen bonds (yellow dashes) are for O-O distances  $< 3 \text{ \AA}$ . **e**, Slices through the isosurfaces, in the absence of an applied potential, of the outer four-helix bundle of the experimental octamer (left) and for models of a parallel hexamer (centre) and an antiparallel hexamer (right) of  $K_2$ -CCTM- $V_bI_c$ . These are coloured from red to blue for  $-8 k_bT/e_c$  to  $8 k_bT/e_c$ , and indicate internal negative electrostatic potentials consistent with cation selectivity. **f,g**, Calculated electrostatic potential energies for moving  $K^+$  (purple) and  $Cl^-$  (green) through the channels of the outer four-helix bundle (**f**) and the hexameric models (**g**; parallel, solid lines; antiparallel, dotted lines). **h**, Calculated channel radii for the outer four-helix bundle of the octamer (blue), the hexameric models (parallel, orange; antiparallel, grey). **i**, Calculated I-V curves for the four-helix bundle (blue), the hexamers (parallel, orange; antiparallel, grey), with the experimental data shown as points.

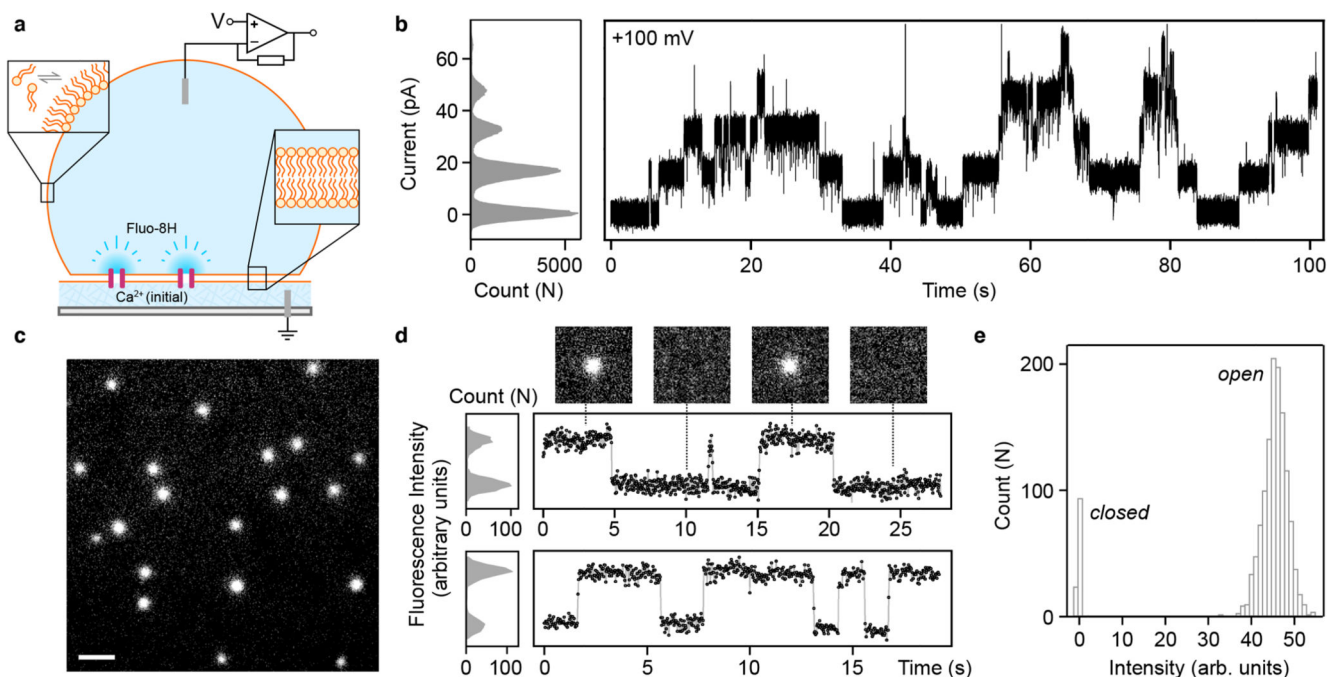


**Fig. 4. CCTM-V<sub>b</sub>I<sub>c</sub> channels in droplet-interface bilayers.**

**a.** Cartoon of a DIB formed between an aqueous droplet and a hydrogel substrate spun onto a coverslip (grey), both in the presence of a lipid-in-oil solution. The DIB has Ca<sup>2+</sup> ions in the hydrogel and the Ca<sup>2+</sup>-sensitive dye Fluo-8H in the droplet. Channels (purple blocks) formed in the bilayer allow passage of Ca<sup>2+</sup> ions into the droplet to generate plumes of Ca<sup>2+</sup>-bound dye (depicted in darker blue) that can be imaged using TIRF microscopy. **b.** Conductance steps from multiple insertions of CCTM-V<sub>b</sub>I<sub>c</sub> in a DIB at +100 mV. Voltages are *trans* relative to *cis* (peptide). **c.** oSCR for CCTM-V<sub>b</sub>I<sub>c</sub> channels in a DPhPC membrane at +100 mV. This is a single 30 ms exposure; 100 nM CCTM-V<sub>b</sub>I<sub>c</sub>; scale bar, 10 μm. **d.** Fluorescence intensity versus time traces for two CCTM-V<sub>b</sub>I<sub>c</sub> channels. The y-axes represent mean pixel values of bilayer patches containing the channels. The upper trace is annotated with 30 ms frames (17.8 μm x 17.8 μm) from the respective oSCR image stack. **e.** Spot intensities extracted from eight CCTM-V<sub>b</sub>I<sub>c</sub> channels in the same bilayer, which represent 40 s of open-channel time, show a unitary open state and a closed state. For all experiments, the droplet peptide concentrations were between 25 nM and 100 nM.

**Table 1**  
**Selected *de novo* designed peptide sequences.**

Polar core residues are highlighted bold. All peptides had *N*-terminal acetyl and *C*-terminal amide caps. Green shading indicates a membrane-spanning region. See Supplementary Table 1 for a complete list of peptides used in this study. CC-Type2-(L<sub>a</sub>I<sub>d</sub>)<sub>4</sub> and CC-Type2-(L<sub>a</sub>I<sub>d</sub>S<sub>g</sub>)<sub>4</sub> are described previously as CC-Hept and CC-Hex2.

Name	Sequence	Helical	Binds DPH	Oligomer	PDB Code
Water-soluble	<i>cdefgab cdefgab cdefgab cdefgab cdefgab</i>				
CC-Type2-(L <sub>a</sub> I <sub>d</sub> ) <sub>4</sub>	G EIAKALK EIAKALK EIAWALK EIAKALK G	Yes	Yes	7	4PNA
CC-Type2-(L <sub>a</sub> I <sub>d</sub> S <sub>g</sub> ) <sub>4</sub>	G EIAKSLK EIAKSLK EIAWSLK EIAKSLK G	Yes	Yes	6	4PN9
CC-Type2-(T <sub>a</sub> I <sub>d</sub> ) <sub>2</sub>	G EIAQALK EIAKATK EIAWATK EIAQALK G	Yes	N.D.	6	6YB2
CC-Type2-(T <sub>a</sub> I <sub>d</sub> ) <sub>5</sub>	G EIAQATK EIAQATK EIAKATK EIAWATK EIAQATK G	Yes	Yes	6	6YAZ
CC-Type2-(L <sub>a</sub> T <sub>d</sub> ) <sub>5</sub>	G ETAQALK ETAQALK ETAKALK ETAWALK ETAQALK G	Yes	No	5 – 6	N.D.
CC-Type2-(S <sub>a</sub> I <sub>d</sub> ) <sub>5</sub>	G EIAQASK EIAQASK EIAKASK EIAWASK EIAQASK G	No	N.D.	N.D.	N.D.
CC-Type2-(L <sub>a</sub> S <sub>d</sub> ) <sub>5</sub>	G ESAQALK ESAQALK ESAKALK ESAWALK ESAQALK G	Yes	No	5 – 6	N.D.
CC-Type2-(T <sub>a</sub> S <sub>d</sub> ) <sub>2</sub>	G EIAQALK EIAQALK ESAKATK ESAWATK EIAQALK G	Yes	Yes	6	6YB0
<b>Membrane-soluble</b>	<i>cdefgab cdefgab cdefgab cdefgab</i>	<i>a</i> and <i>d</i> positions line channel/pack core.			
CCTM-L <sub>b</sub> L <sub>c</sub>	KKKKSG <b>ISAWATL</b> <b>LSALATL</b> <b>LSALATL</b> <b>LSAWATL</b> G	<i>e</i> and <i>g</i> positions are interfacial (interior) and help specify the packing of hexamers.			
CCTM-V <sub>b</sub> I <sub>c</sub>	KKKKSG <b>ISAWATV</b> <b>ISALATV</b> <b>ISALATV</b> <b>ISAWATV</b> G	<i>b</i> and <i>c</i> positions are interfacial (exterior) and have a minor role in defining packing.			
K <sub>2</sub> -CCTM-V <sub>b</sub> I <sub>c</sub>	GKK <b>SAWATV</b> <b>ISALATV</b> <b>ISALATV</b> <b>ISAWATV</b> G	<i>b</i> , <i>c</i> and <i>f</i> positions are exterior facing, and thus polar or apolar in water-soluble or membrane-soluble designs, respectively.			
CCTM-I <sub>b</sub> I <sub>c</sub>	KKKKSG <b>ISAWATI</b> <b>ISALATI</b> <b>ISALATI</b> <b>ISAWATI</b> G				
CCTM-I <sub>b</sub> L <sub>c</sub>	KKKKSG <b>ISAWATL</b> <b>ISALATL</b> <b>ISALATL</b> <b>ISAWATL</b> G				